Article

The Final Catalytic Step of Cytochrome P450 Aromatase: A Density Functional Theory Study

John C Hackett, Robert W. Brueggemeier, and Christopher M. Hadad

J. Am. Chem. Soc., **2005**, 127 (14), 5224-5237• DOI: 10.1021/ja044716w • Publication Date (Web): 19 March 2005

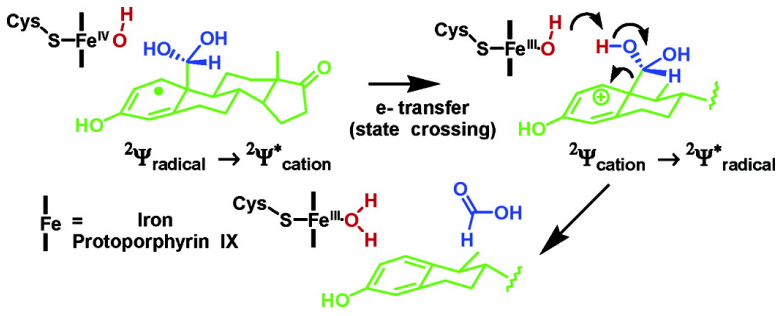

More About This Article

Additional resources and features associated with this article are available within the HTML version:

- Supporting Information
- Links to the 2 articles that cite this article, as of the time of this article download
- Access to high resolution figures
- Links to articles and content related to this article
- Copyright permission to reproduce figures and/or text from this article

View the Full Text HTML

Journal of the American Chemical Society is published by the American Chemical Society. 1155 Sixteenth Street N.W., Washington, DC 20036

J|A|C|S
ARTICLES
Published on Web 03/19/2005

The Final Catalytic Step of Cytochrome P450 Aromatase: A Density Functional Theory Study

John C Hackett,* Robert W. Brueggemeier, and Christopher M. Hadad

Contribution from the Division of Medicinal Chemistry and Pharmacognosy, College of Pharmacy, The Ohio State University, 500 West 12th Avenue, Columbus, Ohio 43210, and the Department of Chemistry, The Ohio State University, 100 West 18th Avenue, Columbus, Ohio 43210

Received September 1, 2004; E-mail: hackett.35@osu.edu

Abstract: B3LYP density functional theory calculations are used to unravel the mysterious third step of aromatase catalysis. The feasibility of mechanisms in which the reduced ferrous dioxygen intermediate mediates androgen aromatization is explored and determined to be unlikely. However, proton-assisted homolysis of the peroxo hemiacetal intermediate to produce P450 compound I and the C19 *gem*-diol likely proceeds with a low energetic barrier. Mechanisms for the aromatization and deformylation sequence which are initiated by 1β-hydrogen atom abstraction by P450 compound **I** are considered. 1β-Hydrogen atom abstraction from substrates in the presence of the 2,3-enol encounters strikingly low barriers (5.3−7.8 kcal/mol), whereas barriers for this same process rise to 17.0−27.1 kcal/mol in the keto tautomer. Transition states for 1β-hydrogen atom abstraction from enolized substrates in the presence of the 19-*gem*-diol decayed directly to the experimentally observed products. If the C19 aldehyde remains unhydrated, aromatization occurs with concomitant decarbonylation and therefore does not support dehydration of the C19 aldehyde prior to the final catalytic step. On the doublet surface, the transition state connects to a potentially labile 1(10) dehydrogenated product, which may undergo rapid aromatization, as well as formic acid. Ab initio molecular dynamics confirmed that the 1β-hydrogen atom abstraction and deformylation or decarbonylation occur in a nonsynchronous, coordinated manner. These calculations support a dehydrogenase behavior of aromatase in the final catalytic step, which can be summarized by 1β-hydrogen atom abstraction followed by *gem*-diol deprotonation.

Introduction

Aromatase (CYP19) is the cytochrome P450 enzyme responsible for the conversion of androgens, including androstenedione and testosterone, to the estrogen products, estrone and estradiol.[1,2] This enzyme plays a key role in the regulation of these sex steroids in reproductive and adipose tissue and may modulate sexual differentiation in the brain.[3] Aromatase has been a particularly attractive target for inhibition in the treatment of hormone-dependent breast cancer since the aromatization of androgen substrates is the terminal and rate-limiting step in estrogen biosynthesis.[3] Inhibitors of this enzyme have proven very efficacious in attenuating this disease.[4] From a mechanistic standpoint, aromatase is very interesting because it is one of a few enzymes capable of constructing an aromatic ring.

Biotransformation of androgens by aromatase proceeds in three oxidative steps, each consuming a single mole of molecular oxygen and NADPH (Scheme 1):

$$\text{Androstenedione (Testosterone)} + 3\text{NADPH} + 3\text{H}^+ + 3\text{O}_2 \rightarrow \text{Estrone (17}\beta\text{-Estradiol)} + \text{HCOOH} + 3\text{H}_2\text{O} + 3\text{NADP}^+$$

The first oxidation occurs at the 19-methyl group (Scheme 1, step a) by the classical enzyme-mediated hydrogen atom abstraction-hydroxyl radical rebound mechanism originally proposed by Groves and co-workers.[5] The first hydroxylation proceeds with retention of configuration.[6] Experiments using [19-^{3}H$_3$]androst-4-ene-3,7-dione show that the small tritium kinetic isotope effect observed with aromatization is exclusively associated with the first hydroxylation step.[7] Studies using the labeled suicide substrate analogue [19-^{3}H$_3$,4-^{14}C]androst-4-ene-3,6,17-trione also revealed a marked tritium isotope effect with the first 19-hydroxylation.[8] The second hydroxylation reaction (Scheme 1, step b) stereoselectively removes the 19-*pro-R*

(1) Ryan, K. J. *Biochim. Biophys. Acta* **1958**, *27*, 658.
(2) Ortiz de Montellano, P. R. Oxygen Activation and Reactivity. In *Cytochrome P450: Structure, Mechanism, and Biochemistry*, 2nd ed.; Ortiz de Montellano, P. R., Ed.; Plenum Press: New York, 1995; pp 245−303.
(3) Brodie, A. M. H. *ISI Atlas of Science: Pharmacology*; Institute for Scientific Information: Philadelphia, PA, 1987; p 266.
(4) (a) Baum, M.; Budzar, A. U.; Cuzik, J.; Forbes, J.; Houghton, J. H.; Klijn, J. G.; Sahmoud, T. *Lancet* **2002**, *359*, 2131. (b) Bonneterre, J.; Buzdar, A.; Nabholtz, J. M.; Robertson J. F.; Thurlimann, B.; von Euler, M.; Sahmoud, T.; Webster, A.; Steinberg, M. *Cancer* **2001**, *92*, 2247. (c) Brueggemeier R. W. *Expert Rev. Anticancer Ther*. **2002**, *2*, 181.
(5) (a) Groves, J. T.; Watanabe, Y. J. *J. Am. Chem. Soc*. **1988**, *110*, 8443. (b) Groves, J. T.; McMurry, T. J. *Rev. Port. Quim*. **1985**, *27*, 102.
(6) (a) Caspi, E.; Arunachalam, T.; Nelson, P. A. *J. Am. Chem. Soc*. **1983**, *105*, 6987. (b) Caspi, E.; Arunachalam, T.; Nelson, P. A. *J. Am. Chem. Soc*. **1986**, *108*, 1847.
(7) (a) Miyairi, S.; Fishman, J. *Biochem. Biophys. Res. Commun*. **1983**, *117*, 392. (b) Miyairi, S.; Fishman, J. *J. Biol. Chem*. **1985**, *260*, 320.
(8) Numazawa, M.; Midzuhashi, K.; Nagaoka, M. *Biochem. Pharmacol*. **1994**, *47*, 717.

10.1021/ja044716w CCC: $30.25

Scheme 1

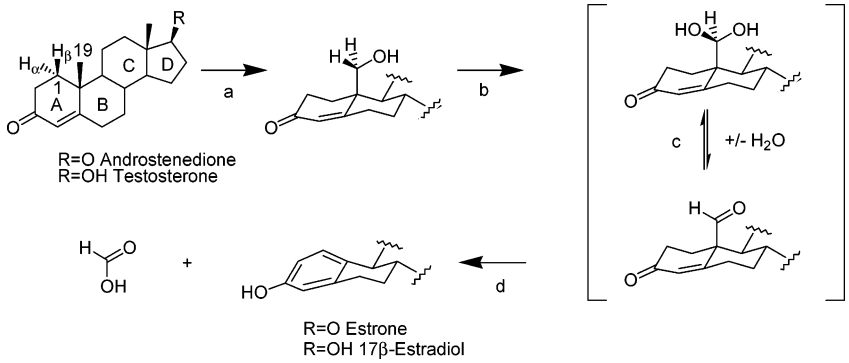

hydrogen without an apparent kinetic isotope effect to yield the 19-*gem*-diol, which may dehydrate to the 19-aldehyde (Scheme 1, step c).[9]

The third step oxidatively cleaves the C10−C19 bond, resulting in aromatization of the steroid A-ring and release of formic acid (Scheme 1, step d). A number of mechanisms have been proposed and shown to be experimentally unlikely. These include 2β-hydroxylation,[10] 4,5-epoxidation,[11] Baeyer−Villiger oxidation of C19,[12] and 10β-hydroxyestr-4-ene-3,17-dione formation.[13] It has been known for many years that the 1β- and 2β-hydrogens are lost stereospecifically to the aqueous medium.[14] A number of model reaction studies have suggested that formation of the 2,3-enol is a prerequisite for aromatization.[15] Differences in the stereoselectivity of the 2-hydrogen atom removal between androstenedione and testosterone indicate that the enzyme mediates the enolization process.[16] A homology model of the aromatase enzyme has been constructed using the X-ray structures of soluble bacterial P450s. The active site model suggests the presence of an aspartic acid residue near the 2β-hydrogen and lysine or histidine residues near the 3-ketone of androstenedione. The orientation of these residues is supportive of an enzyme acid−base catalyzed enolization process to selectively remove the 2β-hydrogen.[17] One mechanism for the oxidative deformylation step that has received significant favor involves nucleophilic attack of the 19-aldehyde by the reduced ferrous dioxygen intermediate (Scheme 2). The resulting peroxo hemiacetal is suggested to decay via a process by which the

Scheme 2

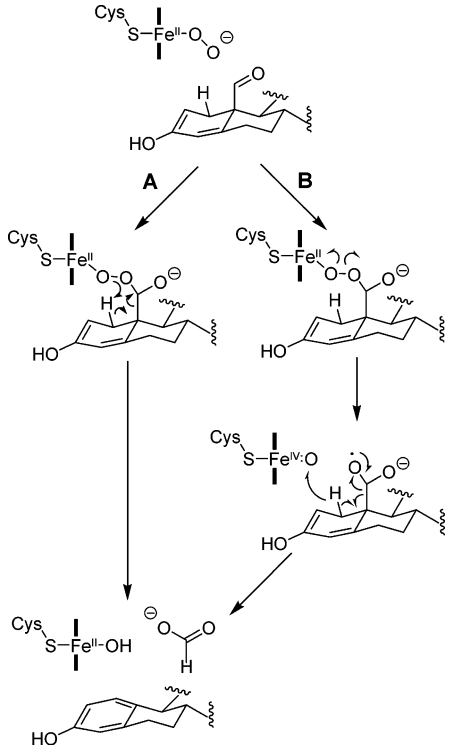

proximal oxygen atom removes the 1β-hydrogen, resulting in aromatization of the steroid A ring and formic acid release.[12] Studies monitoring the incorporation of enzymatically consumed $^{18}O_2$ into the formate product have been performed using crude microsomal preparations containing aromatase.[12] However, these results are open to interpretation since evidence exists that isolated 19-hydroxy and 19-oxo androstenedione metabolites may be products of P450 enzymes other than aromatase.[18]

In this article, a model system of the cytochrome P450 active site and truncated steroid substrates are studied with density functional theory to unravel the mysterious third step of aromatase catalysis. First, the feasibility of the mechanism in which the reduced ferrous dioxygen intermediate mediates androgen aromatization is explored. Second, we consider processes and locate transition states in which the widely accepted P450 oxidant, compound **I** (see Figure 1), abstracts the 1β-hydrogen atom initiating the aromatization and deformylation cascade.

(9) (a) Osawa, Y.; Shibata, K.; Rohrer, D.; Weeks, C.; Duax, W. L. *J. Am. Chem. Soc.* **1975**, *97*, 4400. (b) Arigoni, D.; Battaglia, R.; Akhtar, M.; Smith, T. *J. Chem. Soc., Chem. Commun.* **1975**, 185.
(10) (a) Hosoda, H.; Fishman, J. *J. Am. Chem. Soc.* **1974**, *96*, 7325. (b) Goto, J.; Fishman, J. *Science* **1977**, *195*, 80. (c) Fishman, J.; Raju, M. S. *J. Biol. Chem.* **1981**, *256*, 4472. (d) Hahn, E. F.; Fishman, J. *J. Biol. Chem.* **1984**, *259*, 1689. (e) Caspi, E.; Wicha, J.; Arunachalam, T.; Nelson, P.; Spiteller, G. *J. Am. Chem. Soc.* **1984**, *106*, 7282.
(11) (a) Morand, P.; Williamson, D. G.; Layne, D. S.; Lompa-Krzymien, L.; Salvador, J. *Biochemistry* **1975**, *14*, 635. (b) Mastalerz, H.; Morand, P. *J. Chem. Soc., Perkin Trans. 1* **1982**, 2611.
(12) Akhtar, M.; Calder, M. R.; Corina, D. L.; Wright, J. N. *Biochem. J.* **1982**, *201*, 569.
(13) (a) Covey, D. F.; Hood, W. R.; Beusen, D. D.; Carrell, H. L. *Biochemistry* **1984**, *23*, 5398. (b) Townsley, J. D.; Possanza, G. J.; Brodie, H. J. *Fed. Proc.* **1966**, *25*, 282; Abstract 520. (c) Caspi, E.; Dharmaratne, H. R. W.; Shackleton, C. *J. Chem. Soc., Chem. Commun.* **1989**, 1699.
(14) (a) Brodie, H. J.; Kripalani, K. J.; Possanza, G. *J. Am. Chem. Soc.* **1969**, *91*, 1241. (b) Fishman, J.; Guzik, H. *J. Am. Chem. Soc.* **1969**, *91*, 2805. (c) Fishman, J.; Guzik, H.; Dixon, D. *Biochemistry* **1969**, *8*, 4304.
(15) (a) Cole, P. A.; Robinson, C. H. *J. Chem. Soc., Chem. Commun.* **1986**, *1651*. (b) Cole, P. A.; Robinson, C. H. *J. Chem. Soc., Perkin Trans. 1* **1990**, 2119. (c) Cole, P. A.; Robinson, C. H. *J. Am. Chem. Soc.* **1988**, *110*, 1284. (c) Cole, P. A.; Bean, J. M.; Robinson, C. H. *Proc. Natl. Acad. Sci. U.S.A.* **1990**, *87*, 2999.
(16) Cole, P. A.; Robinson, C. H. *Biochem. J.* **1990**, *268*, 553.
(17) Graham-Lorence, S.; Amarneh, B.; White, R. E.; Peterson, J. A.; Simpson, E. R. *Protein Sci.* **1995**, *4*, 1065.
(18) Bednarski, P. J.; Nelson, S. D. *J. Steroid Biochem.* **1989**, *32*, 309.

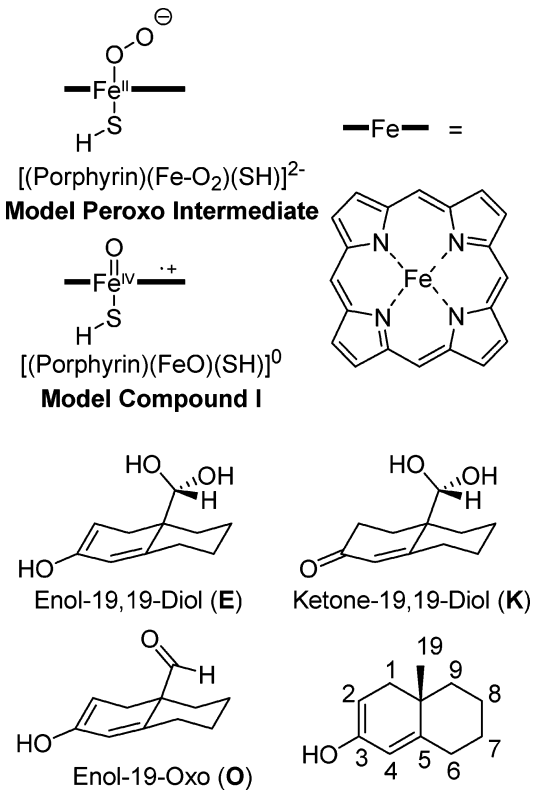

Figure 1. Model systems and the androstane-based numbering system used in this study.

Computational Methodology

Model Systems and Nomenclature. The reduced ferrous dioxygen intermediate and compound **I** of cytochrome P450 were modeled as $[(\text{Porphyrin})(\text{Fe}-\text{O}_2)(\text{SH})]^{2-}$ and $[(\text{Porphyrin})(\text{FeO})(\text{SH})]^0$ complexes, respectively (Figure 1). QM/MM investigations by Shaik and co-workers including the full protoporphyrin IX and steric and electric field contributions of the apoprotein reveal that this truncated system may be a reliable mimic for computationally intensive mechanistic studies.[19] The aromatase enzyme aromatizes the A ring of steroid substrates androstenedione and testosterone. These substrates are considerably large for full quantum mechanical treatment, especially in combination with the P450 model systems. In this study, we are exclusively interested in the chemical transformation that occurs in the A ring of the steroid system. Atoms in the C and D rings of the substrate are sufficiently distant and likely have minimal influence on the computed relative energetics of stationary points on the aromatization potential energy surface (PES). For this reason, the *trans*-decalin structures displayed in Figure 1 are employed, which share common structural features with the A and B rings of the steroid substrates. The hydration status of the doubly oxidized substrate that participates in the third catalytic step and the point in the enzymatic transformation that the prerequisite tautomerization occurs are unknown. These facts suggested the use of three model steroid systems. The first two represent the enol and keto tautomers of the hydrated form of the steroid and therefore contain the 19,19-*gem*-diol functional group (Scheme 1, step c). The third model is in the enol form likely necessary for aromatization, although it contains the 19-aldehyde to explore the possibility of this hydration status to produce the experimentally observed products.

Herein, three steroid model systems and two spin multiplicity PESs are investigated, and therefore a myriad of species are discussed. To simplify the discussion, a simple nomenclature will be laid out to aid the reader in navigating through the article (Figure 1). Each species will be identified unless noted otherwise with a three-letter code preceded by a numerical superscript indicating its spin multiplicity. The first letter will indicate the substrate (**E** = enol-19,19-*gem* diol, **K** = keto-19,19-*gem* diol, and **O** = enol-19-oxo), and the second pair of letters will identify this species' place on the PES. **RS** = reactant supermolecule (reactants separated by infinite distance), **RC** =van der Waals complex of reactants, **TS** = transition state, **PC** = van der Waals complex of products, **PS** = product supermolecule, and **HR** = hydroxyradical intermediate. For example, ^{2}**ETS** is the transition state of the enol-19,19-*gem*-diol model steroid on the doublet potential energy surface.

Theoretical Methods

The systems were studied with the unrestricted hybrid density functional theory method UB3LYP,[20] as defined in the *Gaussian 03* suite in which the VWN functional III is used instead of functional V.[21] Geometry optimizations of transition states and minima were computed with the *Gaussian 03* suites of programs[22] and utilized the TZV[23] basis set for iron and the 3-21G* basis set[24] for the remaining atoms. The 3-21G* basis set is comparatively small relative to those recently used to study P450 model systems, but in this study proves to produce geometric parameters comparable to similar species previously described in the literature.[25] In addition, this basis set is a reasonable choice to bring ab initio molecular dynamics (AIMD) within reach of the computational resources available. Unless otherwise noted, properties (i.e., barrier heights, spin densities) of the optimized species were derived from single-point energy computations using the Wachter's + f [26,27] basis set for iron and the 6-311+G**[28] basis set for the remaining

(19) Schöneboom, J. C.; Lin, H.; Reuter, N.; Thiel, W.; Cohen, S.; Ogliaro, F.; Shaik, S. *J. Am. Chem. Soc.* **2002**, *124*, 8142.

(20) (a) Stevens, P. J.; Devlin, F. J.; Chablowski, C. F.; Frisch, M. J. *J. Phys. Chem.* **1994**, *98*, 11623. (b) Becke, A. D. *J. Chem. Phys.* **1993**, *98*, 5648. (c) Becke, A. D. *J. Chem. Phys.* **1992**, *96*, 2155. (d) Becke, A. D. *J. Chem. Phys.* **1992**, *97*, 9173. (e) Lee, C.; Yang, W.; Parr, R. G. *Phys. Rev. B* **1988**, *37*, 785.

(21) Vosko, S. H.; Wilk, L.; Nusair, M. *Can. J. Phys.* **1980**, *58*, 1200.

(22) Frisch, M. J.; Trucks, G. W.; Schlegel, H. B.; Scuseria, G. E.; Robb, M. A.; Cheeseman, J. R.; Montgomery, J. A., Jr.; Vreven, T.; Kudin, K. N.; Burant, J. C.; Millam, J. M.; Iyengar, S. S.; Tomasi, J.; Barone, V.; Mennucci, B.; Cossi, M.; Scalmani, G.; Rega, N.; Petersson, G. A.; Nakatsuji, H.; Hada, M.; Ehara, M.; Toyota, K.; Fukuda, R.; Hasegawa, J.; Ishida, M.; Nakajima, T.; Honda, Y.; Kitao, O.; Nakai, H.; Klene, M.; Li, X.; Knox, J. E.; Hratchian, H. P.; Cross, J. B.; Adamo, C.; Jaramillo, J.; Gomperts, R.; Stratmann, R. E.; Yazyev, O.; Austin, A. J.; Cammi, R.; Pomelli, C.; Ochterski, J. W.; Ayala, P. Y.; Morokuma, K.; Voth, G. A.; Salvador, P.; Dannenberg, J. J.; Zakrzewski, V. G.; Dapprich, S.; Daniels, A. D.; Strain, M. C.; Farkas, O.; Malick, D. K.; Rabuck, A. D.; Raghavachari, K.; Foresman, J. B.; Ortiz, J. V.; Cui, Q.; Baboul, A. G.; Clifford, S.; Cioslowski, J.; Stefanov, B. B.; Liu, G.; Liashenko, A.; Piskorz, P.; Komaromi, I.; Martin, R. L.; Fox, D. J.; Keith, T.; Al-Laham, M. A.; Peng, C. Y.; Nanayakkara, A.; Challacombe, M.; Gill, P. M. W.; Johnson, B.; Chen, W.; Wong, M. W.; Gonzalez, C.; Pople, J. A. *Gaussian 03*, revision B.04; Gaussian, Inc.: Pittsburgh, PA, 2003.

(23) (a) Schaefer, A.; Horn, H.; Ahlrichs, R. *J. Chem. Phys.* **1992**, *97*, 2571. (b) Schaefer, A.; Huber, C.; Ahlrichs, R. *J. Chem. Phys.* **1994**, *100*, 5829.

(24) (a) Binkley, J. S.; Pople, J. A.; Hehre, W. J. *J. Am. Chem. Soc.* **1980**, *102*, 939. (b) Gordon, M. S.; Binkley, J. S.; Pietro, W. J.; Hehre, W. J. *J. Am. Chem. Soc.* **1983**, *104*, 2797. (c) Pietro, W. J.; Francl, M. M.; Hehre, W. J.; Defrees, D. J.; Pople, J. A.; Binkley, J. S. *J. Am. Chem. Soc.* **1982**, *104*, 5039. (d) It is important to note that the 3-21G* basis set only has polarization functions for second-row atoms, and therefore such polarization functions are only available to sulfur in this study.

(25) (a) Shaik, S.; Cohen, S.; de Visser, S. P.; Sharma, P. K.; Kumar, D.; Kozuch, S.; Ogliaro, F.; Danovich, D. *Eur. J. Inorg. Chem.* **2004**, 207. (b) Loew, G. H.; Harris, D. L. *Chem. Rev.* **2000**, *100*, 407. (c) Harris, D. L. *Curr. Opin. Chem. Biol.* **2001**, *5*, 724 and references therein.

(26) (a) Wachters, A. J. H. *J. Chem. Phys.* **1970**, *52*, 1033. (b) Wachters, A. J. H. *IBM Tech. Rept.* **1969**, RJ584. (c) Bauschlicher, C. W.; Langhoff, S. R.; Barnes, L. A. *J. Chem. Phys.* **1989**, *91*, 2399.

(27) Basis sets were obtained from the Extensible Computational Chemistry Environment Basis Set Database, version 02/25/04, as developed and distributed by the Molecular Science Computing Facility, Environmental and Molecular Sciences Laboratory, which is part of the Pacific Northwest Laboratory, P.O. Box 999, Richland, WA 99352, USA, and funded by the U.S. Department of Energy. The Pacific Northwest Laboratory is a multiprogram laboratory operated by Battelle Memorial Institute for the U.S. Department of Energy under contract DE-AC06-76RLO 1830. Contact David Feller or Karen Schuchardt for further information.

(28) (a) Krishnan, R.; Binkley, J. S.; Seeger, R.; Pople, J. A. *J. Chem. Phys.* **1980**, *72*, 650. (b) Clark, T.; Chandrasekhar, J.; Schleyer, P. v. R. *J. Comput. Chem.* **1983**, *4*, 294.

atoms. Spherical harmonic basis functions (i.e., 5d, 7f) were used in all calculations. Minima were verified to have all real vibrational frequencies, and transition states had a single imaginary vibrational frequency. These frequency analyses also provided the necessary parameters to compute zero-point vibrational energy corrections. The effect of a low dielectric continuum ($\epsilon = 5.621$) on the electronic structure of these systems and their relative energetics were evaluated with the polarizable continuum model (PCM) of Tomasi and coworkers.[29] We believe the dielectric constant of this solvent is a reasonable approximation of the environment experienced by the heme center at the protein active site. In many of the computations including this solvation model, unbound hydrogen atoms, or those transferred as the complex proceeds to products, were treated explicitly for their contribution to the solute cavity. This approximation has been applied in a number of elegant studies to investigate the consequences of a polarized environment on the structure and reactivity of P450 compound **I**.[30]

Some of the reaction mechanisms described in this study are concerted, in which a complex series of transformations occur in an apparently barrierless fashion on the path from 1β-hydrogen atom abstraction to eventual product formation. Unfortunately, intrinsic reaction coordinate[31] calculations on complexes described here with such a large number of active internal coordinates are computationally intractable. As an alternative, AIMD simulations were carried out on the Born−Oppenheimer potential energy hypersurface in the *Turbomole 5.6* suite of programs.[32,33] To initialize each AIMD run, 1β-hydrogen atom abstraction transition-state geometries were used for the initial atomic positions and random velocities were applied at 310.15 K. A time step, Δt, of 40 au (0.97 fs) was chosen. This time step is approximately one order of magnitude smaller than the shortest vibrational period of the system (the O−H stretch, 9.5 fs). Some simulations were repeated with a 20 au time step, which traced out nearly identical trajectories, validating the choice of a longer, and computationally convenient, time step. The wave function was fully converged, and the gradient was computed at each time step at the B3LYP/(TZV,3-21G*) level of theory. The Leapfrog Verlet algorithm[34] propagated the nuclear coordinates along the dynamical trajectory for 200 time steps:

$$r(t + \Delta t) = r(t) + \Delta t v(t + \Delta t/2)$$

$$v(t + \Delta t/2) = v(t - \Delta t/2) + \Delta t[f(t)/m]$$

Important geometries that correspond to inflection points on the molecular dynamics energy profiles were characterized with single-point energy calculations using the TZVP[23] basis set for iron and the SV(P)[23] basis set for the remaining atoms in the gas phase with *Turbomole*. Single-point energies of the geometries in the presence of a low-dielectric continuum ($\epsilon = 5.621$) with the PCM model were computed in *Gaussian 03*.

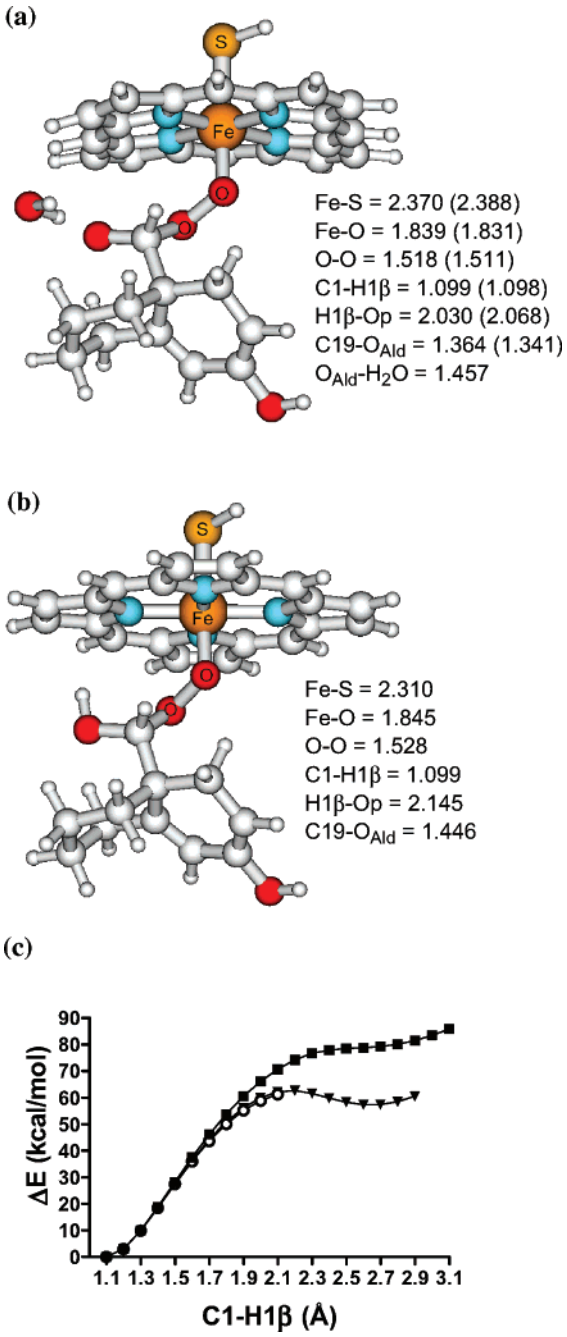

Figure 2. Structure of the hydrated peroxo hemiacetal adduct of the (a) enol-19-oxo steroid and (b) protonated peroxo hemiacetal adduct. O_{Ald} denotes the aldehyde oxygen, and distances are given in angstroms. Geometric parameters for the unhydrated species are in parentheses. (c) Results of the B3LYP/(TZV,3-21G*) C1−H1β PES scans. Protonated (■), hydrated (○), and unhydrated (▼) peroxo hemiacetal adducts are plotted with regard to the C1−H1β bond distance.

Population analyses were carried out with the natural population analysis (NPA)[35] and Mulliken methods. Time-dependent density functional theory (TD-DFT) calculations at the B3LYP/(TZVP,SV(P)) level of theory were carried out with the ESCF module[36] of the *Turbomole 5.6* suite of programs.

(29) (a) Miertus, S.; Scrocco, E.; Tomasi, J. *J. Chem. Phys.* **1981**, *55*, 117. (b) Miertus, S.; Tomasi, J. *Chem. Phys.* **1982**, *65*, 39. (c) Cossi, M.; Barone, V.; Cammi, R.; Tomasi, J. *Chem. Phys. Lett.* **1996**, *255*, 327.
(30) (a) Ogliaro, F.; Cohen, S.; de Visser, S.; Shaik, S. *J. Am. Chem. Soc.* **2000**, *122*, 12892. (b) Ogliaro, F.; de Visser, S.; Cohen, S.; Sharma, P. K.; Shaik, S. *J. Am. Chem. Soc.* **2002**, *124*, 2806. (c) de Visser, S. P.; Ogliaro, F.; Sharma, P. K.; Shaik, S. *J. Am. Chem. Soc.* **2002**, *124*, 11809. (d) de Visser, S. P.; Shaik, S. *J. Am. Chem. Soc.* **2003**, 125, 7413. (e) Sharma, P. K.; de Visser, S. P.; Shaik, S. *J. Am. Chem. Soc.* **2003**, *125*, 8698. (f) de Visser, S. P.; Shaik, S.; Sharma, P. K.; Kumar, D.; Thiel, W. *J. Am. Chem. Soc.* **2003**, *129*, 15779. (g) Ogliaro, F.; de Visser, S. P.; Cohen, S.; Kaneti, J.; Shaik, S. *ChemBioChem* **2001**, *11*, 848.
(31) (a) Gonzalez, C.; Schlegel, H. B. *J. Chem. Phys.* **1989**, *90*, 2154. (b) Gonzalez, C.; Schlegel, H. B. *J. Phys. Chem.* **1990**, *94*, 5523.
(32) (a) Ahlrichs, R.; Bär, M.; Häser, M.; Horn, H.; Kölmel, C. *Chem. Phys. Lett.* **1989**, *162*, 165. (b) For the current version of TURBOMOLE, see http://www.turbomole.de.
(33) A description of the ab initio molecular dynamics code implemented in the FROG module of *Turbomole 5.6* can be found in: Elliott, S. D.; Ahlrichs, R.; Hampe, O.; Kappes, M. M. *Phys. Chem. Chem. Phys.* **2000**, *2*, 3415.
(34) Verlet, L. *Phys. Rev.* **1967**, *159*, 98.
(35) Reed, A. E.; Weinstock, R. B.; Weinhold, F. *J. Chem. Phys.* **1985**, *83*, 735.
(36) (a) Weiss, H.; Ahlrichs, R.; Häser, M. *J. Chem. Phys.* **1993**, *99*, 1262. (b) Bauernschmitt, R.; Ahlrichs, R. *Chem. Phys. Lett.* **1996**, *256*, 454. (c) Bauernschmitt, R.; Häser, M.; Treutler, O.; Ahlrichs, R. *Chem. Phys. Lett.* **1997**, *264*, 573.

Scheme 3

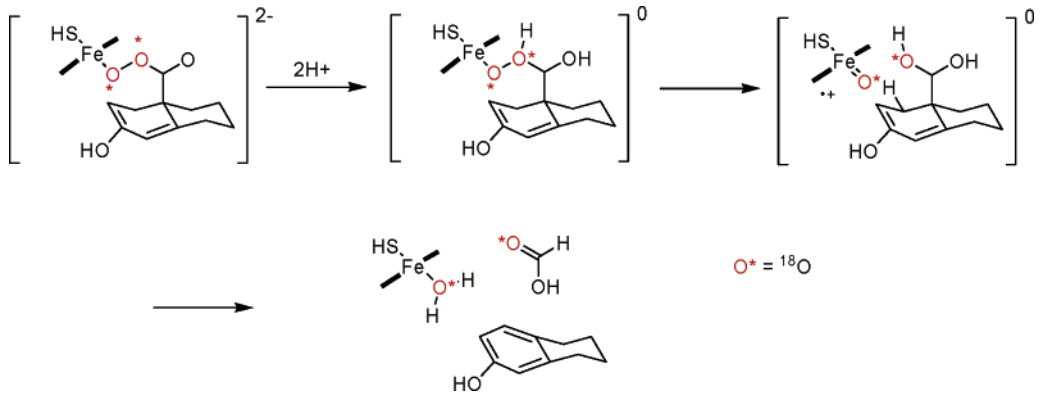

Results and Discussion

Deformylation by the Ferrous Peroxo Intermediate. A mechanism that has remained consistent with all available experimental aromatase data was proposed by Akhtar and involves attack of the reduced ferrous dioxygen intermediate on C19 of the 19-oxo enolized steroid.[12] The resulting peroxo hemiacetal intermediate is believed to fragment into the aromatized product, formic acid, and a hydroxo ferric enzyme intermediate that may be rapidly protonated leaving the aqua-bound P450. (Scheme 2, path A) To study whether the operation of this mechanism in the final catalytic step of aromatase is feasible, we constructed and optimized models of the ferrous peroxo hemiacetal intermediate with the enolized substrate and performed rigid PES scans of the C1−H1β distance coordinate to estimate the barrier of hydrogen-atom abstraction by the proximal oxygen of the ferrous peroxo unit.

Three models of the ferrous peroxo hemiacetal intermediate were constructed and optimized at the B3LYP/(TZV,3-21G*) level of theory. Structures and key geometric parameters are displayed in Figure 2. Only the doublet state was considered in these studies since previous density functional theoretical work in our laboratory with extended models of the P450 active site have indicated this to be the ground state and well-separated from the higher-lying quartet state. Previous computations using models including a cysteinamide ligand and the 6-31G(d) basis set with the B3LYP, BP86, and BPW91 functionals revealed that the doublet state was separated from the quartet by 6.7−11.5 kcal/mol in the gas phase and 16.6−17.5 kcal/mol with a dielectric continuum of $\epsilon = 5.621$.[37] Two models are dianionic, one with a water molecule hydrogen-bonded to the aldehyde oxygen. In the third model, the aldehyde oxygen is protonated with a net system charge of −1. Formation of the unhydrated and hydrated dianionic models from their isolated components was 31.7 and 67.8 kcal/mol exothermic, respectively.[38] The rigid PES scans of the C1−H1β coordinate were conducted in 0.1 Å increments, the energies of which are plotted relative to that of the respective ferrous peroxo hemiacetal reactant (Figure 2c). Results of the PES scans are supportive of very high barriers for hydrogen-atom abstraction by the proximal oxygen (O_p). For the protonated species, the PES briefly plateaus at approximately 80 kcal/mol when the C1−H1β coordinate is 2.6 Å, placing the hydrogen atom 1.3 Å from O_p. Further scanning does not provide evidence of an additional potential energy well beyond this point. Complete geometry optimization of the species with C1−H1β equal to 2.6 Å returns to the reactant complex. PES scans of the same coordinate in the unhydrated and singly hydrated analogue support lower barriers (~60 kcal/mol) for 1β-H abstraction by the proximal oxygen; however, these values are still too immense to be accessible by enzymatic catalysis. The approximate barrier for hydrogen atom abstraction from the dianionic species is 63 kcal/mol and occurs at a C1−H1β distance of 2.2 Å where the H1β−O_p distance is 1.2 Å. SCF convergence difficulties prevented scanning beyond a C1−H1β value of 2.1 Å in the singly hydrated intermediate. The potential energy curve prior to this value followed that of the unhydrated species identically, indicating that hydrogen bonding to the aldehyde oxygen has no impact on the 1β-H abstraction barrier. In the unhydrated complex, a shallow potential energy well is encountered at 2.6 Å and H1β−O_p of 1.12 Å. Geometry optimization from this well does not result in fragmentation to the experimentally observed products or return to reactants; alternatively, it optimizes to a stable, proximal-oxygen protonated species.

The possibility that the aromatization reaction is initiated by an iron peroxo O−O bond homolysis, thereby generating a compound **II** intermediate ([(Porphyrin)(FeO)(SH)]$^{1-}$) and a steroid substrate radical oxyanion, has also been considered. After O−O homolysis, it is possible that the oxyanion radical could decompose to formate and the model steroid radical, the latter of which could be subject to 1β-hydrogen atom abstraction by compound **II** leading to the experimentally observed products (Scheme 2, path B). Indeed, fragmentation of the model steroid oxyanion radical to the formate anion and a C10 radical is favored energetically. However, PES scans of the O−O coordinate are supportive of approximate high barriers for homolysis of ~33 kcal/mol and >42 kcal/mol for the unprotonated and protonated species, respectively, thereby rendering these pathways to be noncompetitive. O−O homolysis is exothermic (~−22 kcal/mol) in the unprotonated intermediate only when the ^{3}A state of compound **II** is formed.

In contrast to the approximate high O−O homolysis barriers obtained with the unprotonated and aldehyde oxyanion protonated models, protonation of the aldehyde oxyanion and the distal oxygen provides a route to the widely accepted P450 oxidant compound **I** and the enol-19,19-diol species (Scheme

(37) Hackett, J. C.; Brueggemeier, R. W.; Hadad, C. M. *J. Phys. Chem. B*, submitted for publication.
(38) We were unable to perform a rigid PES scan of the distal oxygen−C19 coordinate for the initial attack of C19 by the model intermediate due to problems with self-consistent field equation convergence.

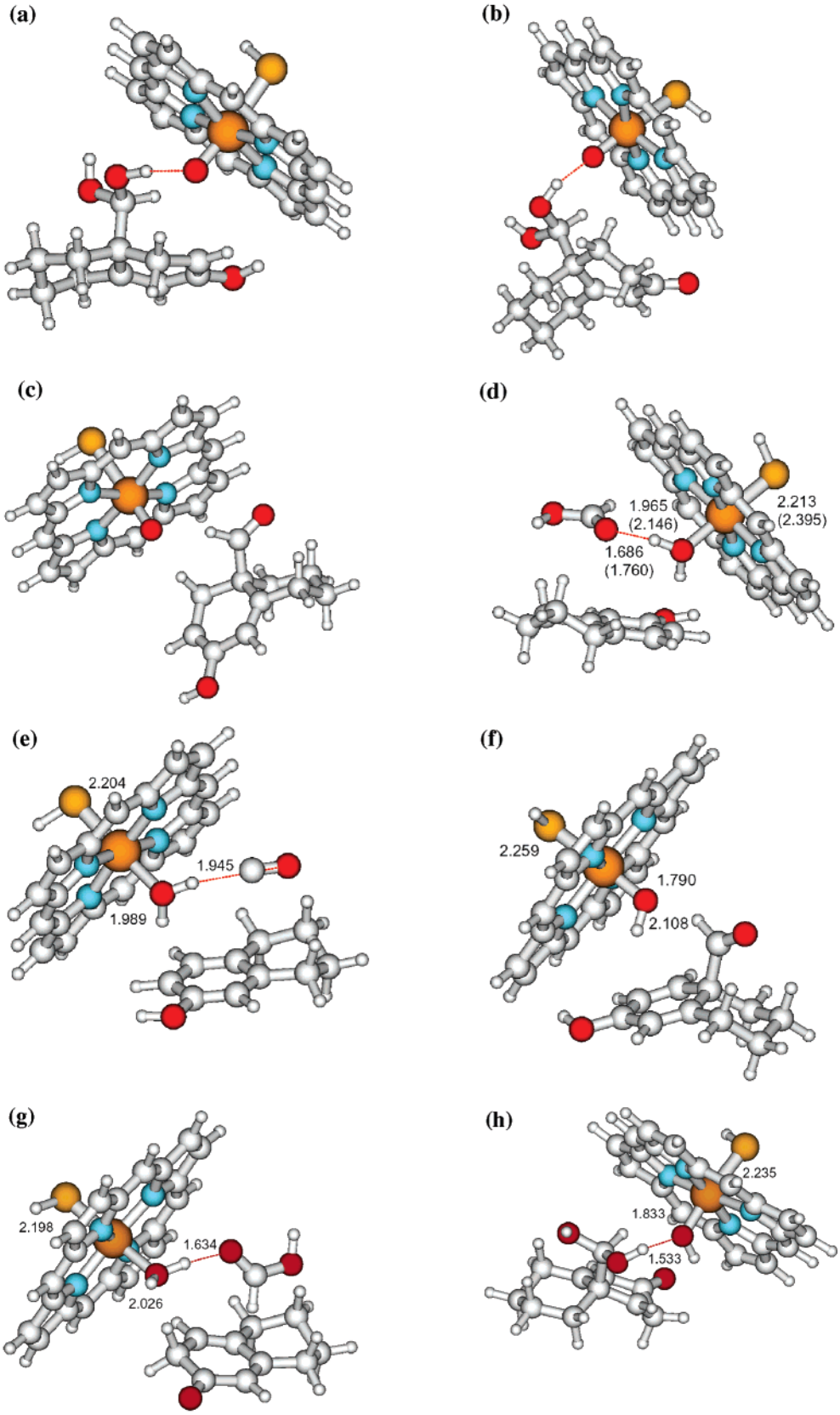

Figure 3. Fully optimized structures of (a) **^{2}ERC**, (b) **^{2}KRC**, (c) **^{2}ORC**, (d) **^{2,4}EPC**, (e) **^{2}OPC**, (f) **^{4}OHR**, (g) **^{2}KPC**, and (h) **^{4}KHR** at the B3LYP/(TZV,3-21G*) level of theory. Selected distances are given in angstroms. Quartet surface values are given in parentheses.

3). Distal oxygen protonation of the protonated aldehyde oxyanion model, followed by full optimization at the B3LYP/(TZV,3-21G*) level of theory, verifies that this is a stable, neutral intermediate. Homolysis of the O−O bond to form compound **I** and the enol-19,19-diol is mildly exothermic (∼−0.4 kcal/mol). A PES scan of the O−O coordinate reveals

Table 1. Bond Lengths (in Å) and Angles (in Degrees) for the ^{2}A(^{4}A) Reactant Clusters and 1β-Hydrogen Atom Abstraction Transition States[a]

Geometric Parameter	^{2}ERC (^{4}ERC)	^{2}ETS (^{4}ETS)	^{2}KRC (^{4}KRC)	^{2}KTS (^{4}KTS)
Fe−O	1.664 (1.676)	1.715 (1.732)	1.656 (1.658)	1.810 (1.781)
Fe−S	2.447 (2.408)	2.324 (2.298)	2.455 (2.459)	2.288 (2.268)
Fe−N	2.007 (2.007)	2.010 (2.010)	2.004 (2.003)	2.003 (2.001)
$H^{1\beta}$−O(Fe)	2.413 (2.487)	1.601 (1.484)	2.537 (2.524)	1.129 (1.226)
C1−$H^{1\beta}$	1.093 (1.091)	1.158 (1.186)	1.096 (1.096)	1.447 (1.359)
∠(Fe)O−$H^{1\beta}$−C1	127.2 (115.2)	170.6 (173.0)	140.8 (141.5)	146.4 (154.4)
O−H^{pro-S}−O(Fe)	1.616 (1.610)	1.437 (1.484)	1.657 (1.671)	1.533 (1.596)
O−H^{pro-S}	1.020 (1.023)	1.068 (1.052)	1.015 (1.014)	1.044 (1.028)
O−H^{pro-R}	0.996 (0.997)	0.997 (0.997)	0.997 (0.997)	0.997 (0.997)

Geometric Parameter	^{2}ORC (^{4}ORC)	^{2}OTS (^{4}OTS)
Fe−O	1.652 (1.658)	1.689 (1.730)
Fe−S	2.479 (2.477)	2.359 (2.312)
Fe−N	2.004 (2.004)	2.006 (2.005)
$H^{1\beta}$−O(Fe)	2.190 (2.145)	1.526 (1.414)
C1−$H^{1\beta}$	1.103 (1.103)	1.174 (1.222)
∠(Fe)O−$H^{1\beta}$−C1	165.1 (166.2)	170.8 (171.1)
$H^{aldehyde}$−(Fe)	2.140 (2.176)	1.984 (1.988)
$C^{aldehyde}$−H	1.104 (1.104)	1.104 (1.102)

[a] The quartet surface value is listed in parentheses.

an approximate barrier for homolysis of ∼10 kcal/mol. These data indicate that, if indeed the peroxo intermediate is operative in the final catalytic step of aromatase and proceeds through a peroxo hemiacetal intermediate, the aforementioned prerequisite proton-assisted mechanism provides a favorable reaction channel for its decay to generate the observed formate product. In addition, this fragmentation mechanism is consistent with the ^{18}O atom distribution in products observed by Akhtar and coworkers wherein only one ^{18}O label appears in the formate product.[12] Details of these computations are provided in the Supporting Information.

In light of the apparently high energetic barriers for mechanistic processes in which the peroxo intermediate directly mediates aromatization, we have considered the possibility that compound **I** may be an active oxidant in the final step of aromatase catalysis. Given that 2β-hydrogen loss to the aqueous medium can be accounted for by a 2,3-enolization step prerequisite for aromatization, we have considered several mechanisms of aromatization that are initiated by 1β-H abstraction by compound **I**. Because of the lack of knowledge regarding the 2,3-tautomeric and C19 hydration status during this catalytic step, these possibilities have been incorporated into the model systems. The results of these studies are discussed next.

The Model Steroid−Compound I Complexes. The electronic structure of P450 compound **I** has been a flourishing debate between theoreticians over the past decade, although more recently a working consensus has evolved.[30a,i,39] There is now widespread agreement that compound **I** has two closely lying spin states. Each state has two electrons in a triplet configuration localized to the FeO moiety, while a third electron resides in an orbital of mixed porphyrin π and sulfur p character from the distal thiolate ligand. The contributing porphyrin π orbital shares similar properties to the highest-lying a_{2u} orbital of iron porphyrin in D_{4h} symmetry. Antiferromagnetic and ferromagnetic coupling of the electron in this mixed character orbital to the FeO triplet pair gives rise to nearly degenerate doublet and quartet states, respectively. The optimized geometries of **^{2}ERC**, **^{2}KRC**, and **^{2}ORC** are representative of these geometries on both the doublet and quartet spin surfaces and are displayed in Figure 3a−c. Critical geometric parameters for these species and the ^{4}A−^{2}A energetic spacings are listed in Tables 1 and 2, respectively. The geometries of these species were identified by distorting the reaction vector in the corresponding 1β-hydrogen atom transition state toward reactants as discussed below and subjecting the system to full optimization. Geometric parameters for the [(Porphyrin)(FeO)(SH)] component of the reactant complexes are in agreement within the estimated experimental uncertainty with the crystal structure of oxyferrous cytochrome P450cam.[40] The complexes identified here have doublet and quartet states separated by small energetic spacings (<∼1.5 kcal/mol) whose values are listed in Table 2.

Table 2. ^{4}A−^{2}A Energetic Splitting for Reactant Complexes[a]

theory	ERC	KRC	ORC
B3LYP/(TZV, 3-21G*)	−1.64	0.33	0.04
B3LYP/(TZV, 3-21G*) + ZPE	−1.33	0.42	0.10
B3LYP/(Wachter's + f, 6-311+G**)[b]	−0.08	0.39	0.22
PCM (ϵ = 5.621)-B3LYP/ (Wachter's + f, 6-311+G**)[b]	1.11	0.62	0.12

[a] A negative value for the high spin−low spin splitting indicates that the high spin is favored. [b] Single-point energy computation using the B3LYP/(TZV,3-21G*) fully optimized geometry.

RC spin densities illustrating these intermediates generally share the same electronic structure properties as species studied previously. Group and atomic charges and spin densities illustrating this point are listed in Table 3. Fe and O atomic spin densities indicate the presence of two parallel, unpaired electrons centered on these atoms. In the cases of **^{2,4}KRC** and **^{2,4}ORC**, a third antiferromagnetically or ferromagnetically coupled electron to the triplet pair is shared between the porphyrin macrocycle and the thiolate ligand. No appreciable spin density (population) accumulates on the substrate in these cases. In contrast, **^{2,4}ERC** has spin density parallel to that localized to the porphyrin and the thiolate ligand appearing on the model steroid. Analysis of the singly occupied Kohn−Sham orbital of **^{2}ERC** (see Supporting Information) indicates that the accumulation of spin density on the substrate arises from mixing

(39) (a) Du, P.; Loew, G. H. *Int. J. Quantum Chem*. **1992**, *44*, 251. (b) Antony, J.; Grodzicki, M.; Trautwein, A. X. *J. Phys. Chem. A* **1997**, *101*, 2692. (c) Green, M. T. *J. Am. Chem. Soc*. **1999**, *121*, 7939. (d) Ogliaro F.; de Visser, S. P.; Groves, J. T.; Shaik, S. *Angew. Chem., Int. Ed.* **2001**, *40*, 3503.

Table 3. **^{2,4}ERC**, **^{2,4}KRC**, and **^{2,4}ORC** B3LYP/(Wachter's + f, 6-311+G**) NPA Group and Atomic Charges as Well as Spin Densities[a]

	^{2}ERC	^{4}ERC	^{2}ORC	^{4}ORC	^{2}KRC	^{4}KRC
			Charges			
Fe	0.95 (0.95)	0.93 (0.93)	0.94 (0.95)	0.94 (0.95)	0.93 (0.94)	0.92 (0.94)
O	−0.57 (−0.58)	−0.59 (−0.60)	−0.56 (−0.59)	−0.56 (−0.58)	−0.48 (−0.53)	−0.48 (−0.52)
porphyrin	−0.40 (−0.09)	−0.45 (−0.27)	−0.28 (−0.18)	−0.27 (−0.17)	−0.36 (−0.23)	−0.34 (−0.21)
SH	−0.15 (−0.24)	−0.16 (−0.27)	−0.07 (−0.15)	−0.09 (−0.17)	−0.10 (−0.19)	−0.12 (−0.21)
substrate	0.17 (0.04)	0.28 (0.21)	−0.03 (−0.03)	−0.02 (−0.03)	0.02 (0.01)	0.02 (0.01)
			Spin Densities			
Fe	1.20 (1.23)	1.13 (1.15)	1.16 (1.19)	1.09 (1.11)	1.09 (1.14)	1.02 (1.06)
O	0.81 (0.78)	0.84 (0.83)	0.86 (0.83)	0.91 (0.88)	0.90 (0.86)	0.97 (0.93)
porphyrin	−0.35 (−0.64)	0.24 (0.42)	−0.46 (−0.55)	0.45 (0.55)	−0.42 (−0.53)	0.43 (0.54)
SH	−0.45 (−0.36)	0.41 (0.31)	−0.56 (−0.47)	0.54 (0.45)	−0.57 (−0.46)	0.54 (0.44)
substrate	−0.22 (0.00)	0.37 (0.29)	0.00 (0.00)	0.00 (0.00)	−0.01 (0.00)	0.03 (0.03)

[a] Values computed in the presence of the PCM model with $\epsilon = 5.621$ are in parentheses.

of an antibonding π^* orbital localized on the diene system with the a_{2u} porphyrin/sulfur p orbital. The presence of a low dielectric continuum increases the porphyrin's spin density for these intermediates and diminishes the thiolate spin density. Inclusion of the solvation model has effects on the spin density localized to the substrate of **^{2,4}ERC**. β-Spin density is abolished from the substrate portion of **^{2}ERC** in the presence of solvation, significantly enhancing the porphyrin's radical character. **^{4}ERC** retains the substrate-centered spin density, although it is also slightly decreased in favor of the porphyrin radical.

The 1β-Hydrogen Atom Abstraction and Aromatization Sequence. Transition states for 1β-hydrogen atom abstraction from the substrates on the doublet and quartet spin surfaces were computed, and representative **^{2}ETS**, **^{2}KTS**, and **^{2}OTS** transition-state structures are displayed in Figure 4. A complete list of critical geometric parameters is provided in Table 1. Computed energy profiles for the enol and keto species are shown in Figure 5 and for the 19-oxo species in the Supporting Information. The relative energetics compared to the **RC** on the unique PESs are listed in Table 4.

Hydrogen-atom abstraction from the enol-19,19-diol species (i.e., **^{2}ETS** and **^{4}ETS**) occurs with an exceptionally low energetic barrier (Table 4), and the barriers are 7.5 and 7.8 kcal/mol on the doublet and quartet surfaces, respectively. Inclusion of a dielectric continuum with $\epsilon = 5.621$ lowers these barriers to 5.9 and 5.3 kcal/mol, now with a slight preference for the quartet state. Consideration of zero-point vibrational energy contributions lowers these barriers even further by 2.3 and 2.5 kcal/mol on the doublet and quartet surfaces, respectively. Inspection of **^{2,4}ETS** geometries reveals that this reaction proceeds with an "early" transition state consistent with its energetic similarity to the reactant complex. This is illustrated by the minimal lengthening of the C1−H1β bond in the transition state, compared to the corresponding value in the reactant complexes (see Table 1).

Two possible sources for these strikingly low energy barriers in these model systems were considered. In **^{2,4}ETS** , the *pro-S* 19-OH forms an apparent hydrogen bond with the ferryl oxygen. As a result, the *pro-S* O−H distance (1.068 Å) is slightly longer than the *pro-R* OH (0.997 Å) in **^{2}ETS**. To investigate the role of this hydrogen bond in stabilizing the hydrogen-atom abstraction transition states, this bond was frozen to the value observed for the *pro-R* OH and single-point energies were computed. These frozen O−H barrier heights are listed in Table 4 in brackets and demonstrate little impact on the abstraction barrier height. It appears that stabilization of the transition states of **^{2,4}ETS** species lies principally with the substrate itself. Spin densities of A-ring carbon atoms in the transition states (Figure 4) and the derived substrate C1 radicals (Supporting Information) are delocalized over the entire ring, with the most prominent spin density appearing on the C2 and C5 atoms.

Connection of the **^{2,4}ETS** transition states to the **^{2,4}EPC** (Figure 3d) complexes indicates that this is a very exothermic process, as would be expected with a significant driving force of aromatization. The transition states on both spin surfaces are directly connected to a product complex consisting of the experimentally observed aromatized product, formic acid, and the resting aqua complex of the model enzyme. The identification of these pairs of well-defined intermediate states indicates that, after 1β-hydrogen atom abstraction, concomitant transfer of the *pro-S* hydrogen of the C19 *gem*-diol occurs in an apparently barrierless (concerted) manner to the hydroxy iron intermediate. The imaginary vibrational frequency in Figure 6a is consistent with hydrogen-atom transfer from C1 to compound **I**; however, the normal mode for the imaginary vibrational frequency lacks any significant motion of the *pro-S* hydroxyl group of the *gem*-diol. Therefore, each hydrogen transfer does not occur in a synchronized manner, rather in two nonsynchronous distinct steps. A more detailed discussion of the electronic details of the second hydrogen transfer will be discussed later in the article. Noting this observation, we also tried to identify a similar transition state in which the *pro-R* hydrogen would be poised for transfer to give the experimentally observed products. Several trials failed to produce the desired stationary point, although all of our partial optimizations toward this goal decayed to the same trio of products.

The 19-oxo metabolites of aromatase substrates have been isolated as potential catalytic intermediates in the biosynthesis of estrogens. However, no experimental evidence exists supporting the presence of either the 19,19-*gem*-diol or the dehydrated 19-oxo species at the enzyme active during catalysis site. As part of our initial hypothesis, we envisioned the possibility that, after 1β-hydrogen atom abstraction from the dehydrated intermediate, the steroid A-ring might aromatize, concomitantly liberating the formyl radical. This species was then expected to rebound to the ferric hydroxy radical intermediate leading to the experimentally observed products. To investigate this possibility, we identified the 19-oxo 1β-hydrogen

(40) Schlicting, I.; Berendzen, J.; Chu, K.; Stock, A. M.; Maves, S. A.; Benson, D. E.; Sweet, R. M.; Ringe, D.; Petsko, G. A.; Sligar, S. G. *Science* **2000**, *287*, 1615.

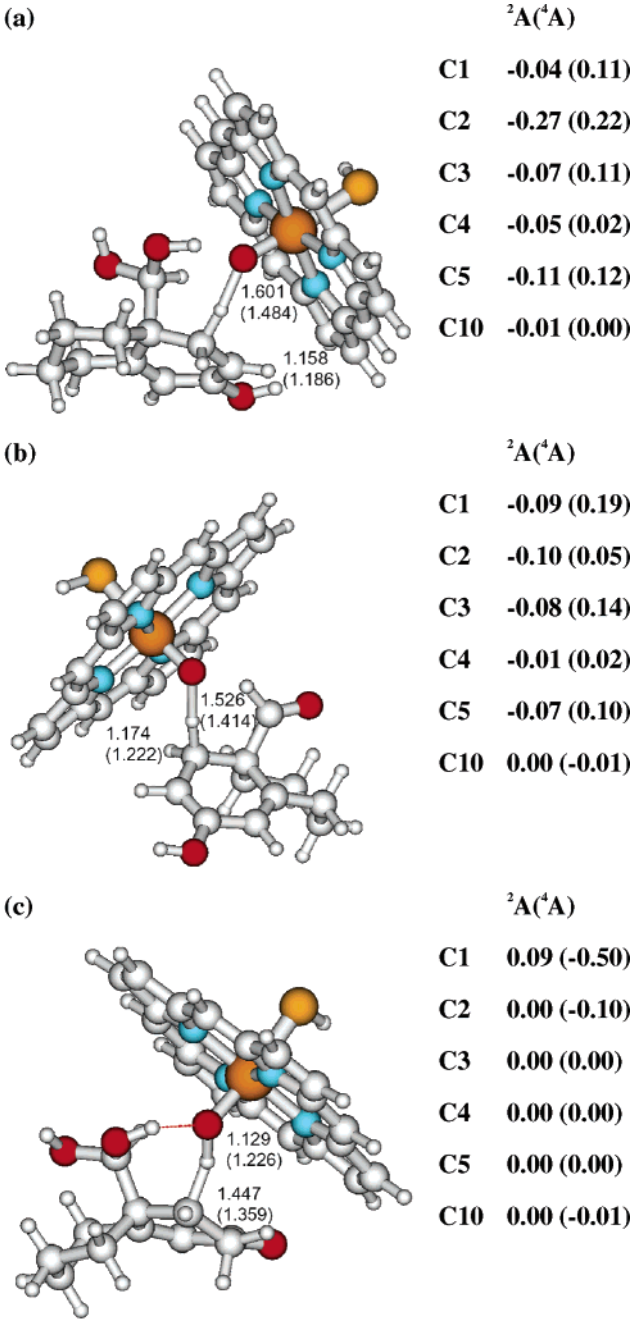

Figure 4. B3LYP/(TZV,3-21G*) fully optimized transition-state structures and A-ring carbon B3LYP/(Wachter's + f, 6-311+G**) NPA spin densities of (a) **^{2}ETS**, (b)**^{2}OTS**, and (c) **^{2}KTS**. C1−H1β and H1β−O(Fe) distances are given in angstroms. The quartet surface value is in parentheses.

atom abstraction transition states (**^{2,4}OTS**) on both spin surfaces (Figure 4b). The barrier heights are similar to those computed with the hydrated analogue and are 6.5 and 7.0 kcal/mol on the doublet and quartet surfaces, respectively. These barriers are lowered to 5.3 and 6.8 kcal/mol in the presence of $\epsilon = 5.621$ dielectric field. Inclusion of zero-point vibrational energy corrections lowers these barriers by 2.2 and 2.5 kcal/mol. C1−H1β−O(Fe) geometric parameters are similar to those for **^{2,4}ETS**, consistent with an early transition state. The spin densities of the A-ring in the transition states and C1 radical underscore the conclusion that the low barriers are a direct result of the substrate's ability to delocalize the developing radical character. Unlike the hydrated analogue, only **^{2}OTS** decays directly to a product complex containing the aromatic entity. Distortion of the **^{2}OTS** structure along the normal mode for the imaginary vibrational frequency (Figure 6b), which is consistent with hydrogen transfer between C1 and the ferryl oxygen, and optimizing the resulting species toward products proved that the **^{2}OTS** transition state is directly connected to **^{2}OPC** (Figure 3e). The **^{2}OPC** structure is a complex of the aromatized product, carbon monoxide and the ferric porphyrin aqua complex. As hypothesized, the formyl group is liberated from the bicyclic substrate en route to aromatization, but *instead of rebound to formic acid, a ferric hydroxy species abstracts hydrogen from the formyl species, resulting in decarbonylation*. The normal mode for the imaginary vibrational frequency has no significant motion of the 19-oxo hydrogen atom, indicating decarbonylation likely occurs in a second distinct step without an observable barrier. Carbon monoxide production is not observed experimentally; so indeed these calculations are not supportive of a dehydration step following formation of the *gem*-diol and compound **I**. One possible explanation for the exclusive formation of formic acid in the final step is that the protein-active site stabilizes the 19-*gem*-diol, preventing dehydration to the corresponding aldehyde. Otherwise, the aromatase apoprotein, which is not considered here, would be required to play a crucial role in utilizing the formyl intermediate to generate the experimental products. For the quartet surface, **^{4}OTS** encounters an intermediate **^{4}OHR** (Figure 3f) on the PES indicative of a subsequent barrier for formyl rebound or decarbonylation. Analysis of the spin density distribution of **^{4}OHR** shows a low atomic charge localized to the substrate species of 0.02 and 0.03 e in the gas phase and with $\epsilon = 5.621$, respectively, and a substrate spin density of 1.00 e in both environments. These parameters indicate that the intermediate on the quartet surface is a complex of the substrate radical and Fe-bound hydroxy radical intermediate. Elongating the C10−C19 bond distance of this species followed by partial optimization also resulted in the decarbonylation by the ferric hydroxyl radical or hydroxide-bound intermediate. Our efforts to identify a transition state for formyl radical rebound on both spin surfaces repeatedly failed, always decaying via the decarbonylation route to generate carbon monoxide.

Hydrogen-atom abstraction from the keto form of the steroid substrate encounters a significantly higher energetic barrier than the two enolized substrates. The computed barriers for 1β-hydrogen atom abstraction are 26.6 and 23.1 kcal/mol on the doublet and quartet surfaces, respectively. Inclusion of an $\epsilon = 5.621$ dielectric field lowers these barrier heights to 25.1 and 22.9 kcal/mol, respectively. Inclusion of the zero-point vibrational energy correction reduces these values by 4.8 and 4.4 kcal/mol. The energetics for the keto analogue are comparable to those previously computed for ethane[41] and camphor[42] with an analogous model system for the P450 enzyme in which the cysteinate ligand is modeled with a methylthiolate anion. This observation is to be expected, as inspection of the spin densities in **^{2,4}KTS** (Figure 4c) and the isolated C1 radical (Supporting Information) indicates that the developing radical cannot delocalize the impending spin density over the steroid's A ring.

(41) (a) Yoshizawa, K.; Shiota, Y.; Kagawa, Y. *Bull. Chem. Soc. Jpn.* **2000**, *73*, 2669. (b) Yoshizawa, K.; Kagawa, Y.; Shiota, Y. *J. Phys. Chem. B* **2000**, *104*, 12365.
(42) Kamachi, T.; Yoshizawa, K. *J. Am. Chem. Soc.* **2003**, *125*, 4652.

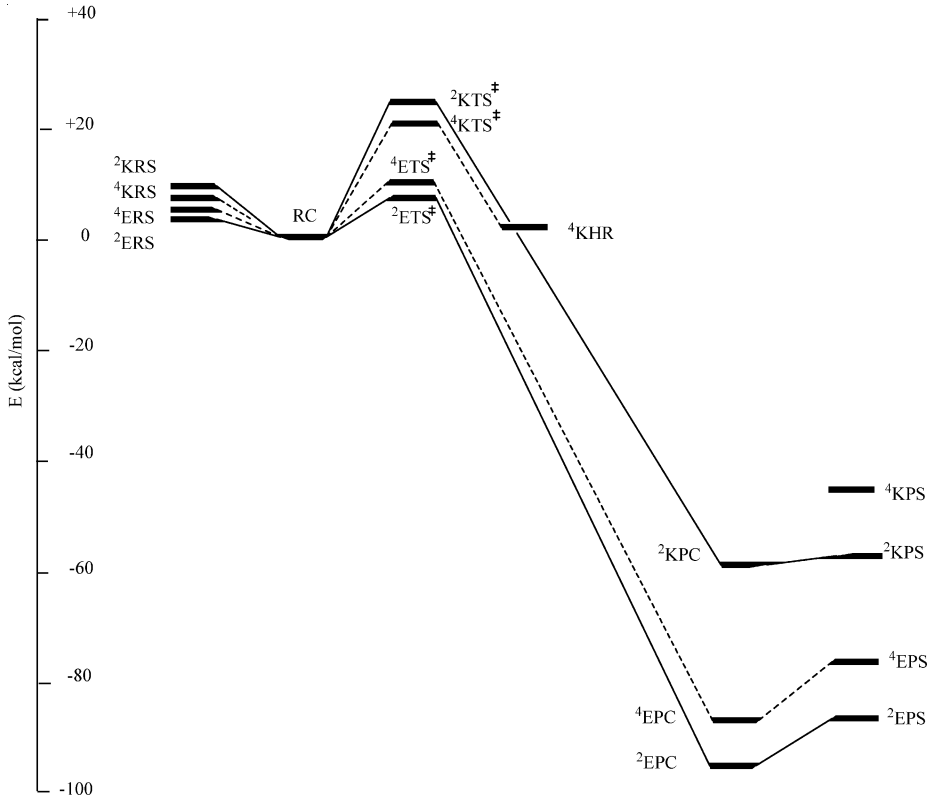

Figure 5. Relative energy diagram of stationary points along the 1β-hydrogen atom abstraction and deformylation reaction for the enol-19,19-diol (**E**) and ketone-19,19-diol (**K**) species at the B3LYP/(Wachter's + f, 6-311+G**)//B3LYP/(TZV,3-21G*) level of theory.

Table 4. Energies Relative to the Reactant Complex of Stationary Points on the ^{2}A (^{4}A)1β-H Atom Abstraction/Aromatization PES[a]

theory	RS	TS	HR	PC	PS
		E			
B3LYP/(TZV,3-21G*)	20.1 (20.8)	4.3 (5.9) [5.5 (6.8)]		−80.2 (−62.4)	−50.1 (−33.9)
B3LYP/(TZV,3-21G*) + ZPE	19.1 (21.6)	2.0 (3.4)		−80.1 (−64.2)	−53.1 (−38.3)
B3LYP/(Wachter's + f, 6-311+G**)	5.6 (5.9)	7.5 (7.8) [6.9 (7.2)]		−94.8 (−88.3)	−88.8 (−76.4)
PCM-B3LYP/(Wachter's + f, 6-311+G**)	−5.6 (−6.7)	5.9 (5.3) [5.4 (4.8)]		−95.2 (−94.6)	−101.6 (−89.6)
		K			
B3LYP/(TZV,3-21G*)	24.6 (24.3)	27.1 (21.4)	(10.1)	−41.9	−15.0 (−0.8)
B3LYP/(TZV,3-21G*) + ZPE	23.1 (22.8)	22.3 (17.0)	(7.5)	−43.9	−20.2 (−7.1)
B3LYP/(Wachter's + f, 6-311+G**)	9.5 (9.3)	26.6 (23.1)	(3.3)	−60.1	−57.0 (−45.1)
PCM-B3LYP/(Wachter's + f, 6-311+G**)	−0.81 (−1.4)	25.1 (22.9)	(3.9)	−65.1	−69.3 (−56.9)
		O			
B3LYP/(TZV,3-21G*)	8.7 (8.7)	3.9 (3.0)	(−14.8)	−70.7	−52.3 (−52.4)
B3LYP/(TZV,3-21G*) + ZPE	8.1 (8.1)	1.7 (0.52)	(−16.2)	−71.6	−55.9 (−56.0)
B3LYP/(Wachter's + f, 6-311+G**)	−0.58 (−0.62)	6.5 (7.0)	(−22.9)	−87.5	−85.2 (−85.4)
PCM-B3LYP/(Wachter's + f, 6-311+G**)	−5.2 (−5.2)	5.3 (6.8)	(−19.1)	−84.3	−88.2 (−88.3)

[a] Energies (kcal/mol) are relative to the reactant complex (**RC**) in each case. See Figure 1 and the text for definitions of the **E**, **K**, and **O** structures. The quartet energetics are listed in parentheses.

^{2}KTS is structurally related to **^{2}KPC** (Figure 3g), which consists of the aqua-ligated model P450, formic acid, and the analogous dehydrogenated 3-oxo-1(10),4-diene product. Although considerably exothermic, the resulting product complex lies 28.7 kcal/mol higher in energy than the doublet surface of the enol tautomer. In contrast, the quartet state encounters **^{4}KHR** (Figure 3h), which indeed can be described as a complex of the substrate radical and hydroxy radical intermediate, as spin density analysis reveals the presence of a full electron (spin density of 1.00 e) localized to the steroid substrate. **^{4}KHR** is only 3−4 kcal/mol below **^{4}KTS**, indicating the presence of a subsequent barrier for secondary hydrogen atom or proton transfer from the model substrate to the hydroxy radical bound to iron. Table 5 shows B3LYP/(Wachter's + f, 6-311+G**) NPA group and atomic charges as well as spin densities for **^{2,4}ETS**, **^{2,4}KTS**, and **^{2,4}OTS**.

Formation of the 1(10) olefin from the keto substrate with energetics similar to those for other cytochrome P450 enzymes that are known to occur is very interesting, and the mechanism described here may have implications in the final step of lanosterol-14α-demethylase (CYP51). This enzyme is responsible for the removal of the 14α-methyl group from lanosterol in the biosynthesis of cholesterol.[43] Like aromatase, the first two hydroxylations appear to be unexceptional hydrogen atom abstraction-hydroxy radical rebound steps yielding the 14α-*gem*-

(43) (a) Alexander, K.; Akhtar, M.; Boar, R. B.; McGhie, J. F.; Barton, D. H. R. *J. Chem. Soc., Chem. Commun*. **1972**, *1972*, 383. (b) Mitropoulos, K. A.; Gibbons, G. F.; Reeves, E. A. *Steroids* **1976**, *27*, 821.

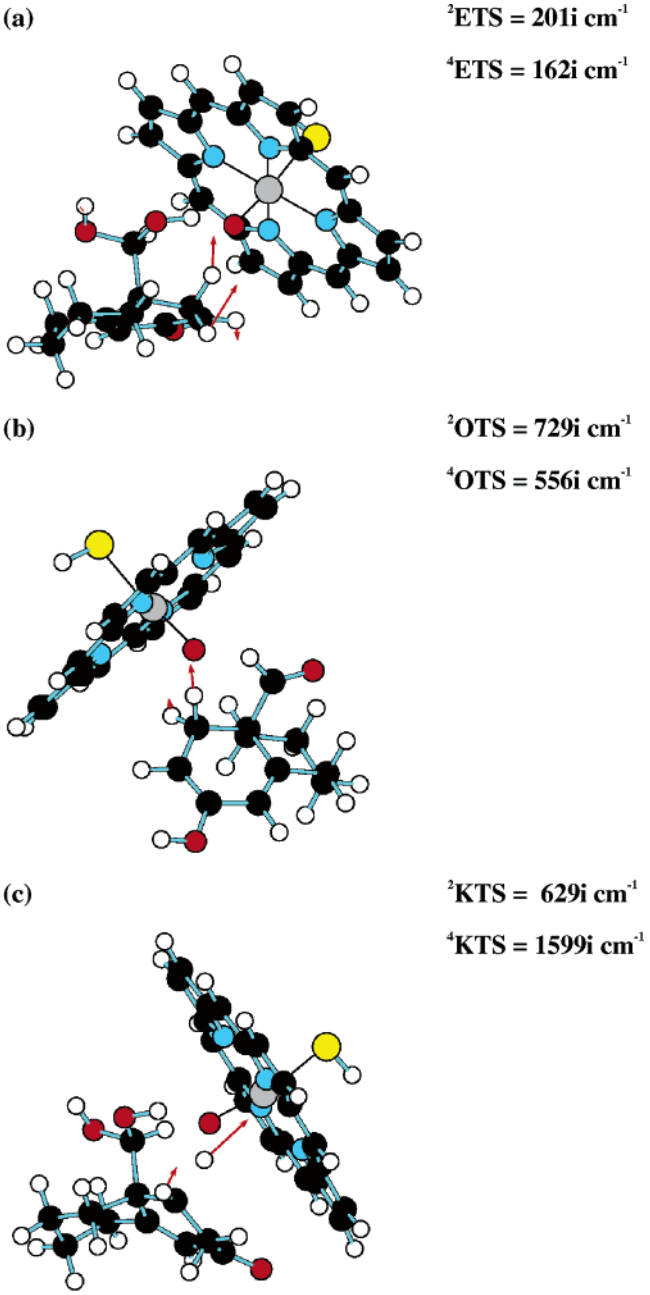

Figure 6. Representative normal modes for the respective imaginary vibrational frequency of the (a) **^{2}ETS**, (b) **^{2}OTS**, and (c) **^{2}KTS** transition-state structures. Displacement vectors are depicted with arrows, and the values for the doublet and quartet states are given.

diol,[44] although the mechanism of the final 15α-hydrogen atom abstraction with concomitant deformylation has also been controversial. In analogy to the mechanism described here, it is possible that the compound **I** intermediate might abstract the 15α-hydrogen atom, yielding the hydroxy radical intermediate. In a subsequent step, a hydrogen atom from the *gem*-diol could be lost to the hydroxyradical intermediate, yielding the experimentally observed mixture of formic acid, the dehydrogenated steroid, and the resting state of the enzyme.

To date, aromatase has resisted structural elucidation by X-ray crystallography, and therefore no template exists in which to construct an expanded QM system or QM/MM system to study the electronic and steric contributions of the protein to aromatization energetics. Full QM/MM studies of the hydroxylation of camphor by cytochrome P450cam have been completed and provide significant insight into the role of the surrounding protein. Guallar et al. studied the 5-*exo* hydrogen-atom abstraction from camphor by the quartet state of P450cam.[45] Their results revealed a 11.7 kcal/mol barrier for hydrogen-atom abstraction (8.2 kcal/mol with zero-point vibrational energy corrections included). When the QM subsystem was extracted from the QM/MM model and the barrier was recomputed in the gas phase, it rose to 20 kcal/mol. This study went on to illustrate the individual steric and electronic contributions of the surrounding protein to the lowering of the barrier. Much of the energetic discrepancy was attributed to electrostatic interactions of the peripheral heme propionate substituents with positively charged amino acid side chains in the pocket, but this is still an area of debate.[19,45]

If the surrounding aromatase apoprotein could be considered here for the derived transition states, we may find the final aromatization step with enolized substrates to have a negligible barrier or be apparently barrierless and the keto substrates dehydrogenated with a minimal barrier. Another possibility that would allow steroid substrates in the keto form to contribute to the pool of aromatized product lies in utilizing the kinetic energy liberated during O−O bond cleavage. Using a model of the P450cam active site which included amino acid side chains proposed to be involved in proton delivery to the distal oxygen of the peroxo intermediate by Sligar,[46] Kamachi and Yoshizawa computed the O−O bond cleavage to be 50 kcal/mol exothermic.[42] A more recent QM/MM study by Guallar and Friesner of these steps in P450cam found that 80 kcal/mol was released in the bond-breaking step alone.[47] As proposed by Kamachi and Yoshizawa,[42] the intermediates involved in dioxygen activation and substrate hydroxylation might decay faster than the system equilibrates; therefore, the kinetic energy released during O−O scission may only be partially transferred to the protein. The remaining kinetic energy may be used by compound **I** to overcome the high potential energy barrier for hydrogen-atom abstraction.

Ab Initio Molecular Dynamics of ^{2,4}ETS and ^{2,4}OTS. As noted earlier, concomitant formation of formic acid occurs directly after C1−H1β hydrogen atom abstraction, and we were interested in examining the mechanistic structures along the reaction path. Therefore, to study the potential energy hypersurface between the hydrogen atom abstraction transition states **^{2,4}ETS** and **^{2,4}OTS** to the respective product complexes, Born−Oppenheimer molecular dynamics was used. A similar strategy was used by Yoshizawa and co-workers to effectively follow the geometric and energetic changes that occur along the ethane to ethanol reaction pathway mediated by a similar model of P450 compound **I**.[48] In this study, we limited our simulations to approximately 200 time steps of ∼1 fs. This time scale was

(44) (a) Alexander, K. T. W.; Akhtar, M.; Boar, R. B.; McGhie, J. F.; Barton, D. H. R. *J. Chem. Soc., Chem. Commun.* **1971**, 1479. (b) Akhtar, M.; Freeman, C. W.; Wilton, D. C.; Boar, R. B.; Copsey, D. B. *Bioorg. Chem.* **1977**, *6*, 473. (c) Akhtar, M.; Alexander, K.; Boar, R. B.; McGhie, J. F.; Barton, D. H. R. *Biochem. J.* **1978**, *169*, 449.
(45) Guallar, V.; Baik, M.-H.; Lippard, S. J.; Friesner, R. A. *Proc. Natl. Acad. Sci. U.S.A.* **2003**, *100*, 6998.
(46) Vidakovic, M.; Sligar, S. G.; Li, H.; Poulos, T. L. *Biochemistry* **1998**, *37*, 9211.
(47) Guallar, V.; Friesner, R. A. *J. Am. Chem. Soc.* **2004**, *126*, 8501.
(48) Yoshizawa, K.; Kamachi, T.; Shiota, Y. *J. Am. Chem. Soc.* **2001**, *123*, 9806.

Table 5. **^{2,4}ETS**, **^{2,4}KTS**, and **^{2,4}OTS** B3LYP/(Wachter's + f, 6-311+G**) NPA Group and Atomic Charges as Well as Spin Densities[a]

	^{2}ETS	^{4}ETS	^{2}OTS	^{4}OTS	^{2}KTS	^{4}KTS
			Atomic Charges			
Fe	0.96 (0.97)	0.94 (0.96)	0.94 (0.96)	0.91 (0.94)	0.90 (0.92)	0.95 (0.96)
O	−0.73 (−0.74)	−0.73 (−0.74)	−0.61 (−0.63)	−0.63 (−0.66)	−0.80 (−0.80)	−0.76 (−0.76)
porphyrin	−0.57 (−0.57)	−0.59 (−0.57)	−0.51 (−0.50)	−0.56 (−0.53)	−0.40 (−0.39)	−0.46 (−0.41)
SH	−0.24 (−0.33)	−0.19 (−0.29)	−0.24 (−0.33)	−0.17 (−0.26)	−0.18 (−0.25)	−0.06 (−0.11)
1β-H	0.34 (0.34)	0.35 (0.36)	0.32 (0.33)	0.34 (0.35)	0.37 (0.37)	0.37 (0.37)
substrate	0.25 (0.33)	0.22 (0.29)	0.09 (0.17)	0.09 (0.16)	0.11 (0.15)	0.32 (0.33)
			Spin Densities			
Fe	1.40 (1.39)	1.34 (1.38)	1.36 (1.36)	0.91 (0.94)	1.13 (1.14)	1.38 (1.42)
O	0.46 (0.50)	0.67 (0.65)	0.39 (0.40)	0.80 (0.76)	0.18 (0.18)	0.61 (0.60)
porphyrin	−0.12 (−0.09)	0.00 (0.00)	−0.18 (0.17)	0.07 (0.07)	−0.36 (−0.32)	0.11 (0.13)
SH	−0.01 (0.01)	0.21 (0.12)	−0.11 (−0.05)	0.29 (0.19)	−0.03 (−0.02)	0.34 (0.29)
1β-H	−0.02 (−0.03)	0.02 (0.02)	−0.01 (−0.02)	0.00 (0.01)	−0.02 (−0.01)	−0.01 (−0.01)
substrate	−0.70 (−0.78)	0.76 (0.82)	−0.43 (−0.52)	0.59 (0.65)	0.09 (0.05)	0.56 (0.57)

[a] Values computed in the presence of the PCM model with $\epsilon = 5.621$ are in parentheses.

more than sufficient for the transition states to decay to products. Moreover, the formation of products occurred in ~50 fs in each simulation. Single trajectory calculations were performed for each system and spin surface. Single trajectories only provide a sampling of the dynamical behavior of this very important enzymatic reaction. These calculations are limited to providing information about the correct reaction pathway and how the electronic structure of the system changes as the reaction proceeds. The computation of accurate thermodynamic parameters requires statistical treatments of data obtained from multiple trajectory runs and are not considered here. However, we were very interested in understanding the electronic structure in the transformation sequence.

Energy profiles for **^{2,4}ETS** and **^{2,4}OTS** are plotted versus time in Figure 7. These plots include time points relevant to product formation, and the full MD energy profiles are reserved for Supporting Information. All simulations decay to the respective products identified in the stationary point evaluations discussed above. The low-spin state of the aqua-bound P450 model produced in all combinations of products is energetically preferable in all simulations in agreement with the experimental low-spin resting state of cytochrome P450 enzymes.[49] Indeed, the doublet state is preferred energetically through the course of both MD trajectories, with the exception of a near degeneracy to the quartet trajectory at some time points.

Dynamics initiated with the **^{2,4}ETS** stuctures corroborate the connection of transition states to the experimentally observed products. The first 26 steps (~24 fs) of simulation are dominated by a decrease in the H1β−O−Fe angle from the transition-state value of 141° to approximately 109°. As the simulation proceeds past step 26, the H1β−O−Fe angle further decreases to ~76° to allow maximal overlap of the oxygen lone pair with the hydrogen-bound *pro-S* hydroxyl group. At step 34 (~32 fs), the hydrogen transfer to the hydroxy-bound Fe is complete, forming the aqua-bound complex. From this point, the H1β−O−Fe angle begins to increase to 109°. *Pro-S* hydrogen transfer is followed by C10−C19 bond fission, releasing formic acid with simultaneous aromatization of the A-ring.

The hydrogen transfer from the *gem*-diol group is very interesting since it is demonstrative of an alternative reaction channel that can be taken by the hydroxy-bound radical intermediate in P450 enzymes other than rebound to give the hydroxylated product. To characterize this as a hydrogen-atom or proton-transfer mechanism, we studied select time points along the preferred doublet trajectory with B3LYP/(TZVP,SV(P)) single-point energy computations. The structures and critical geometric properties of these species are provided in the Supporting Information. Because of program limitations of *Turbomole*, Mulliken atomic charges are used. While

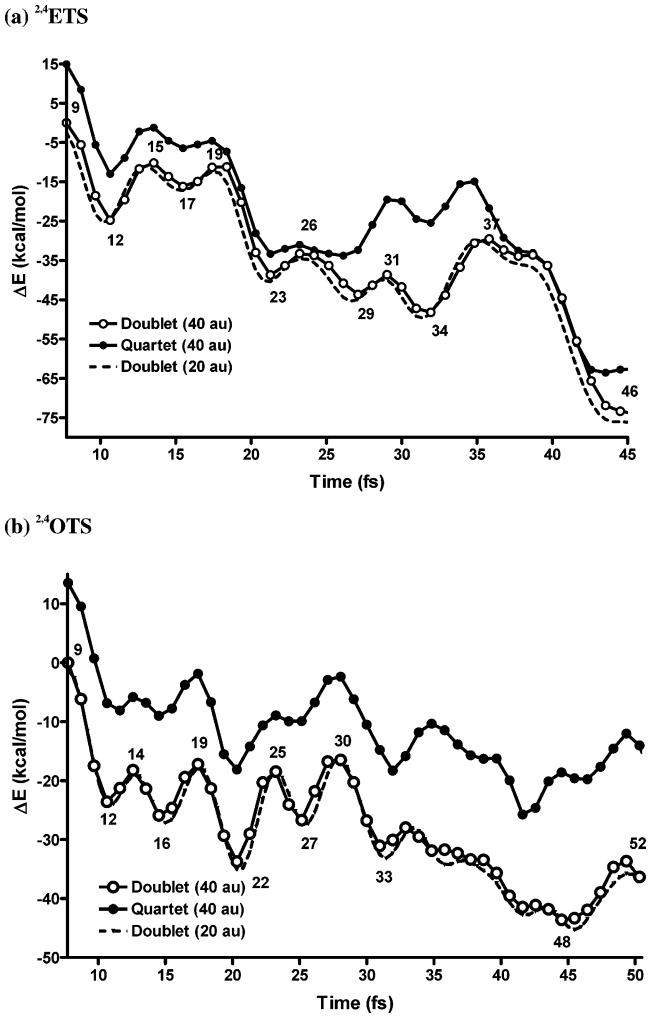

Figure 7. Ab initio MD trajectory energy profiles initiated with (a) **^{2,4}ETS** and (b) **^{2,4}OTS** at the B3LYP/(TZV,3-21G*) level of theory. Only time points relevant to product formation are shown. Structures at time points subjected to B3LYP/(TZVP,SV(P)) single-point energy computations are labeled.

(49) Dawson, J. H.; Sono, M. *Chem. Rev.* **1987**, *87*, 1255.

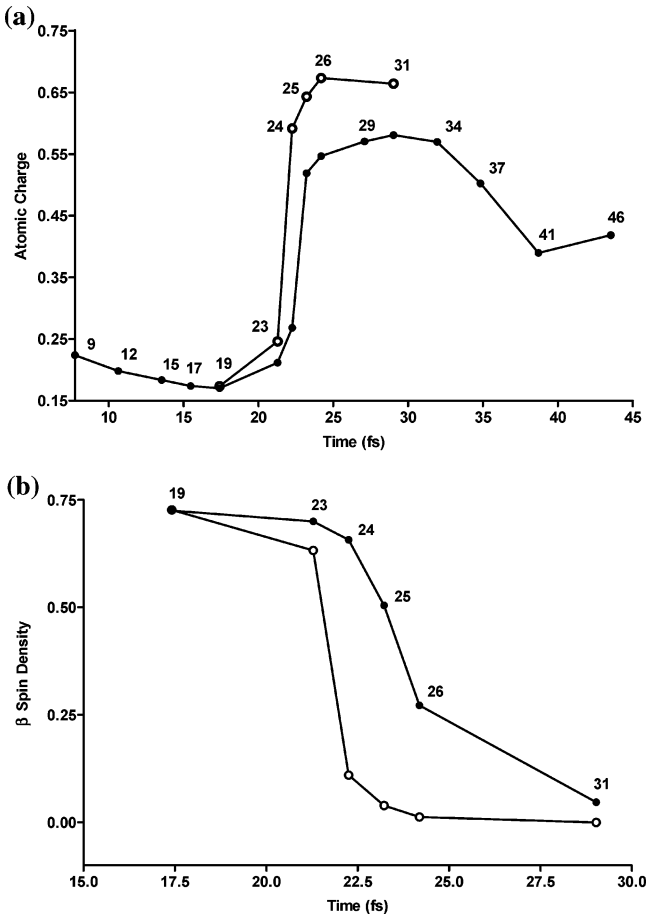

Figure 8. Gas phase (●) and $\epsilon = 5.621$ (○) Mulliken atomic charges (a) and β-spin densities (b) localized on the steroid substrate at critical points on the ab initio MD trajectory for propagation of **^{2}ETS** transition-state structure from Figure 4a.

Mulliken analyses have often been criticized, the qualitative trends identified with these analyses were verified by NPA analysis in *Gaussian* by recomputation of the electronic wave function (see Supporting Information). Figure 8 shows the net Mulliken atomic charge of the substrate at these select time points. From the beginning of the simulation through step 19 (~17 fs), the net atomic charge remains small consistent with a bound substrate radical. The radical nature of step 19 is confirmed with a substrate spin density of 0.7 e. As the simulation proceeds past step 23 (~21 fs), a pronounced accumulation of positive charge occurs on the steroid substrate and reaches a maximum at step 31 (~29 fs), which immediately precedes the hydrogen transfer. With the increase in positive charge on the substrate over this time frame, there is a simultaneous loss of spin density on the substrate. Analysis of the singly occupied molecular orbital (SOMO) of the selected time steps prior to charge accumulation shows that the SOMO is localized exclusively on the substrate. Time steps beyond the charge accumulation are characterized by a SOMO of mixed sulfur/porphyrin π character (Figure 9).

Taken together, the ab initio molecular dynamics results confirm that deformylation to formic acid occurs in two distinct steps. The first is a classical hydrogen-atom abstraction, resulting in formation of the steroid substrate radical. An electron transfer follows from the substrate to the hydroxy radical intermediate. Therefore, the following deformylation step can be most

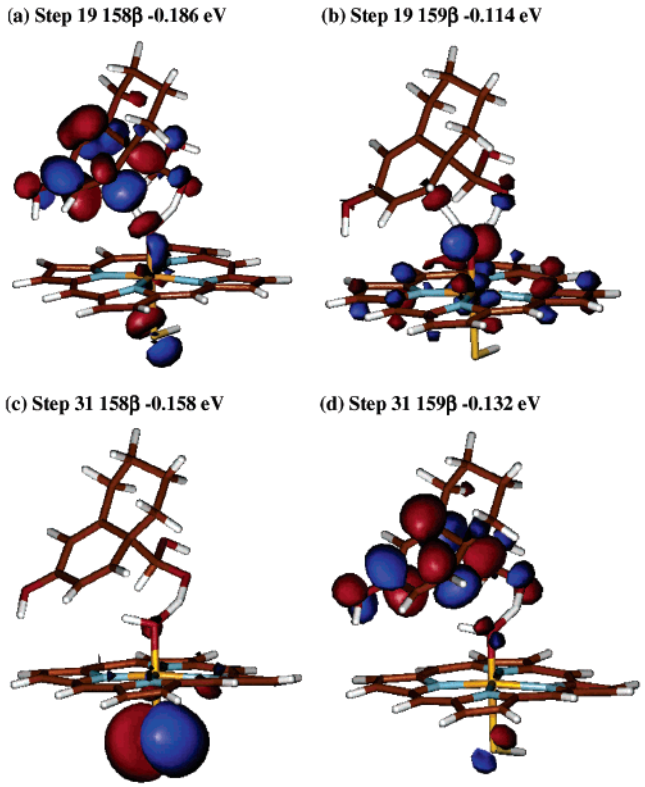

Figure 9. Highest-occupied (158) and lowest-unoccupied (159) β-spin orbitals of the **^{2}ETS** MD steps 19 and 31. A contour value of 0.03 e/B^3 is used.

accurately described as a proton transfer from the substrate cation to the hydroxide-bound P450 intermediate. These steps are outlined in Scheme 4.

We have considered that the apparent electron transfer arises as a result of a substrate cation and substrate radical state crossing as recently described by Kumar et al.[50] To delineate whether this phenomenon occurs in the processes studied here, TD-DFT computations at the B3LYP/(TZVP,SV(P)) level have been employed to study the low-lying excited states of the **^{2}ETS** MD steps 19 and 31, which are akin to a substrate radical and cation, respectively. The step 19 and step 31 structures have low-lying excited states (0.38 and 0.18 eV) whose major contributing configuration is characterized by a transition from the highest-occupied (158) and lowest-unoccupied (159) β-spin orbitals (Figure 9). In the step 19 structure, the lowest excitation is a transition between an antibonding π^* orbital of the substrate diene system and the mixed porphyrin π/sulfur p orbitals, and vice versa for the step 31 structure. As an approximation to the vertical excited-state wave functions, the occupations of the spin orbitals were switched and the populations were recomputed. The substrate Mulliken charges and spin densities for the approximate excited state of the step 19 structure were +0.8 and −0.1 e, respectively, consistent with a cationic excited state. In contrast, the values for the approximate excited state of the step 31 structure were −0.3 and −0.9 e, respectively, consistent with a substrate radical. These results suggest that in the early course of the MD simulation, a substrate radical state is preferred energetically and has a low-lying cationic excited state. As the simulation proceeds, the MD propagates through the state

(50) Kumar, D.; de Visser, S. P.; Shaik, S. *J. Am. Chem. Soc.* **2004**, *126*, 5072.

Scheme 4

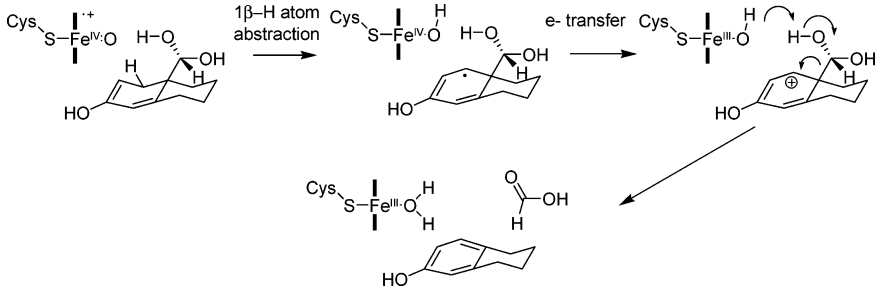

crossing, giving energetic preference to the substrate cation surface and initiating the proton transfer.

Simulations initiated with the ^{2,4}**OTS** geometries confirm that the decarbonylation channel proceeds toward the aromatized product. Following the 1β-hydrogen atom abstraction, the H1β−O−Fe angle equilibrates to nearly 109° and remains near this value until decarbonylation occurs at step 48 (∼45 fs). Prior to decarbonylation, the simulation is dominated by rotation about the Fe−O bond. The 147° rotation orients the hydrogen atom away from the formyl group and repositions the oxygen lone pair for hydrogen transfer from the formyl group. Examination of the relative energetics of specific time points in the vicinity of the actual decarbonylation corroborates the previous PES calculation that the process is apparently barrierless on the doublet surface. B3LYP/(TZVP,SV(P)) single-point energy computations of select geometries along the doublet trajectory confirm a reaction process similar to the hydrated analogue. The charge on the steroid substrate remains low throughout the first 25 steps of MD simulation, consistent with initial hydrogen atom abstraction. As the simulation proceeds past this point, the positive charge on the substrate accumulates to a maximum of +0.60 e immediately preceding the decarbonylation step to generate carbon monoxide. Therefore, an electron transfer followed by formyl deprotonation is operative in this process. Although this mechanism is not functional in the aromatase enzyme, the information gleaned here in combination with future work could contribute to a predictive paradigm for aldehyde metabolism by cytochrome P450.

Conclusions

We have presented a B3LYP density functional theory study of historically accepted and also novel mechanisms for the aromatization and deformylation sequence catalyzed by aromatase. Preliminary studies of peroxo hemiacetal adduct model systems indicate that 1β-hydrogen atom removal by the proximal oxygen of the iron peroxo species requires a high-energy barrier and does not initiate fragmentation to the experimentally observed products. In addition, the previously unconsidered possibility that aromatization occurs via prerequisite O−O homolysis after formation of the peroxo hemiacetal intermediate has been shown to be energetically unfavorable. However, homolysis of the O−O bond in the peroxo hemiacetal intermediate becomes facile when the aldehyde oxyanion and distal oxygens are protonated, producing compound **I** and the *gem*-diol as products.

Alternative mechanistic processes initiated by 1β-hydrogen atom abstraction by the widely accepted ultimate P450 oxidant, compound **I**, were considered. Through these studies, a novel mechanism for the final catalytic step was delineated. A strikingly low barrier height (<7 kcal/mol) for the 1β-hydrogen atom abstraction was computed for steroid models containing the 2,3-enol moiety, and computations using the keto tautomers confirmed the low barrier results from the enolized species' ability to delocalize the developing radical. Noting that the deformylation and dehydrogenation of the keto species occur with similar barriers computed for other known P450 substrates such as camphor, we can speculate that the mechanism described here may be operative in other P450 enzymes where demethylation and dehydrogenation occur with identical oxygen and cofactor requirements.

These studies do not support the dehydration of the 19-*gem*-diol prior to the final catalytic step. Results with model steroids containing the 19-aldehyde are subject to decarbonylation, to yield carbon monoxide, a process that is not consistent with the experimentally observed formic acid product. The characteristics of the ^{2,4}**ETS** reaction vectors and their trajectory for decay to products without subsequent barrier suggest that the second hydrogen removal from the *gem*-diol occurs in a nonsynchronous, coordinated manner. Ab initio molecular dynamics confirmed that both deformylation and decarbonylation occur in two distinct steps. However, removal of the second hydrogen can be more adequately described as a deprotonation of the substrate cation by a ferric hydroxy P450 intermediate formed from a preceding electron-transfer event as depicted in Scheme 4.

Acknowledgment. Computations were carried out at the Ohio Supercomputer Center (OSC) and supported by OSC Grant PAS0091. J.C.H. was supported by USAMRC Predoctoral Fellowship (DAMD17-02-1-0529). C.M.H. acknowledges support from the NSF-funded Environmental Molecular Science Institute (CHE-0089147).

Supporting Information Available: Additional computational data and Cartesian coordinates of the geometries discussed herein. This material is available free of charge via the Internet at http://pubs.acs.org.

JA044716W